



# Combustion behaviors of *Pteris vittata* using thermogravimetric, kinetic, emission and optimization analyses

Yueyao Song<sup>a</sup>, Jingyong Liu<sup>a,\*</sup>, Fatih Evrendilek<sup>b,c</sup>, Jiahong Kuo<sup>a</sup>, Musa Buyukada<sup>d</sup>

<sup>a</sup> Guangzhou Key Laboratory Environmental Catalysis and Pollution Control, Guangdong Key Laboratory of Environmental Catalysis and Health Risk Control, School of Environmental Science and Engineering, Institute of Environmental Health and Pollution Control, Guangdong University of Technology, Guangzhou, 510006, China

<sup>b</sup> Department of Environmental Engineering, Bolu Abant Izzet Baysal University, Bolu, 14052, Turkey

<sup>c</sup> Department of Environmental Engineering, Ardahan University, Ardahan, 75002, Turkey

<sup>d</sup> Department of Chemical Engineering, Bolu Abant Izzet Baysal University, Bolu, 14052, Turkey

## ARTICLE INFO

### Article history:

Received 13 May 2019

Received in revised form

20 July 2019

Accepted 24 July 2019

Available online 25 July 2019

Handling Editor: Sandro Nizetic

### Keywords:

*Pteris vittata*

Thermogravimetric analysis

TG-MS

TG-FTIR

Clean bioenergy generation

Gas pollutants

## ABSTRACT

This study aims to assess the combustion efficiency and emissions of both aboveground (PA) and belowground (PB) biomass parts of *Pteris vittata*. Their combustion process consisted of three major stages, with devolatilization as the main stage of mass loss by 59.06% between 182 and 382 °C for PA, and by 58.24% between 182 and 375 °C for PB. The primary emissions were related to the carbonaceous (90.50% for PA; 90.80% for PB) and N-containing species (6.95% for PA; 6.56% for PB). 172.44% SO<sub>2</sub>, 137.49% NO<sub>2</sub>, and 124.48% CO emissions were released more from the PB than PA combustion. Air pollutants were generated between 70 and 500 °C from PA and 60 and 700 °C from PB, with the PB combustion requiring more pollution controls at a higher temperature. The joint optimizations of derivative thermogravimetry, differential scanning calorimetry, remaining mass, and conversion degree indicated 999.2 and 514.6 °C for combustion temperature, 193.6 and 97.1 min for combustion duration, and 40 °C/min for heating rate as the optimum operational schemes for the PB and PA combustions, respectively. Average activation energy was described using four iso-conversion and integral master-plots methods. The hemicelluloses combustion for PA and PB were best described by the diffusion mechanisms, while the cellulose and lignin + char combustions corresponded to the reaction order mechanisms. Our results contribute to developing the new strategies of cleaner production with the *P. vittata* combustion.

© 2019 Elsevier Ltd. All rights reserved.

## 1. Introduction

Globally, both energy security and environmental benignity of energy supply are closely coupled to human welfare and environmental quality (Wang et al., 2019a). Biomass energy represents about 10% (50 EJ) of the total supply and is the largest renewable source (14%) out of 18% renewables in energy mix (Naqvi et al., 2018). Its share is projected to vary between 55 and 75% of the final energy consumption by 2050 (Paredes-Sanchez et al., 2019). Biomass fuels are abundant in nature, and CO<sub>2</sub>-neutral owing to the balance between C gain via photosynthesis and C loss via respiration, and disturbances (Darda et al., 2019). Biomass has a great affinity with reducing NO<sub>x</sub> emission and capturing CO<sub>2</sub> emission if

used as a fuel through the advanced combustion techniques (Shah et al., 2018). All these factors have motivated a growing interest in the exploration and utilization of alternative biofuels. Different biomass materials have different elemental concentrations whose complex interactions may yield challenges such as air pollution, and corrosion (Magdziarz et al., 2018) as well as opportunities such as catalytic effects when combusted (Yan et al., 2008a). For example, their S and N contents were shown to lead to SO<sub>2</sub>, NO and NO<sub>2</sub> emissions, thus enhancing the acid rain precursors and/or the greenhouse effect (Posom and Sirisomboon, 2017). These quantifications are critical to the choice, design, and application of the industrial-scale combustion technologies.

*Pteris vittata* is a rapidly growing, highly productive and widely geo-distributed plant, and thus, presents a great potential as the biofeedstock for bioenergy generation (Abid et al., 2019). The average annual yield of *P. vittata* was estimated as as high as 36 tons

\* Corresponding author.

E-mail addresses: [Liujiy@gdut.edu.cn](mailto:Liujiy@gdut.edu.cn), [www053991@126.com](mailto:www053991@126.com) (J. Liu).

per hectare (Chen, 2018). *P. vittata* is native to temperate Asia, southern Europe, tropical Africa, and Australia and can even flourish in the hot southern and cold northern environments (Zhang et al., 2017). Therefore, how to handle a large amount of *P. vittata* effectively and properly is of great importance to bio-energy generation, and environmental health (Xie et al., 2009). The biomass combustion as a cost-effective and ecofriendly method accounts for more than 90% of the world's bioenergy production (Bach et al., 2017).

Thermogravimetric (TG) analysis is used in the real-time monitoring of the relationship between (bio)feedstock physico-chemical properties and temperature during the process of combustion, pyrolysis, or torrefaction (Balasundram et al., 2017). TG analysis when integrated with Fourier transform infrared (FTIR) spectrometer can assist in the on-line detection of the functional groups of evolved gases (Wang et al., 2018a). TG and mass spectrometric (TG-MS) analyses also enable the real-time monitoring of temperature-dependent ion current intensity, the identification of key ion signals by mass-to-charge ratio ( $m/z$ ), and the standardization of data by ion current intensity-to-mass ratio ( $A/mg$ ) (Hu et al., 2019). There exist a few studies about the combustion behavior of PA but PB. For example, Lei et al. (2019) studied the reactions of calcium-based adsorbents to capture arsenic during the combustion of arsenic-containing PA. Duan et al. (2017) estimated activation energy ( $E_a$ ) of the combustion and gasification of PA with high arsenic concentration. Yan et al. (2008b) characterized the arsenic transformation and volatilization during the PA incineration by using TG, X-ray absorption spectroscopy and atomic fluorescence spectrometer analyses. There exists a big knowledge gap about the emission characteristics and mechanisms of the PA and PB combustions, controls over air pollution and greenhouse gas emissions. For a cleaner production to be achieved from bio-feedstocks, it is necessary to accurately quantify the combustion parameters, and kinetic responses and barriers.

Therefore, the objectives of this study were to (1) characterize the comparative emission patterns of the PA and PB combustions in the air atmosphere; (2) jointly optimize the multiple responses of derivative TG (DTG), differential scanning calorimetry (DSC), remaining mass (RM), and conversion degree ( $\alpha$ ); and (3) estimate kinetic parameters for the best combustion performances.

## 2. Materials and methods

### 2.1. Preparation and physicochemical analyses of samples

*P. vittata* (also known as Chinese brake fern) was sampled from the Jinbi garden of the Haizhu district in Guangzhou of the Guangdong province, China. The biomass samples were washed with deionized water to remove soil from their roots, sun-dried for 36–48 h and separated into the following two biomass parts of PA (aboveground biomass of leaves and stems), and PB (belowground biomass of stalks and roots). The two parts were ground using a Wiley mill (Marconi MA 048) and sieved to obtain a particle size of less than 74  $\mu\text{m}$ . They were oven-dried at 105 °C for 24 h until reaching a constant weight and maintained in a desiccator for the following tests. Proximate analysis was conducted according to GB/T 2873–2012. An elemental analyzer (Vario eL cube by elemental) was utilized to conduct ultimate analysis. A microcomputer calorimeter (WZR-1T-CII) was used to measure higher heating values (HHV). Results of the above analyses for PA and PB are presented in Table 1.

### 2.2. TG/DSC experiments

A TG analyzer (NETZSCH STA 409 PC) was used to conduct TG/

DSC experiments at 5, 10, 20 and 40 °C/min in the 79% N<sub>2</sub>/21% O<sub>2</sub> (air) atmosphere. The experimental temperature was set to change from 25 to 1000 °C. A blank experiment was conducted at each heating rate to set a baseline to avoid the systematic errors. To realize the reproducibility, the experimental settings were repeated at least twice so as not to exceed a margin of error of  $\pm 2\%$ . In each test,  $6.0 \pm 0.5$  mg of the dry weight samples (weighed using an electronic balance with an accuracy of 0.0001 g) were placed in an alumina crucible, while the furnace was gradually heated to 1000 °C at a gas flow rate of 50 mL/min.

### 2.3. TG-MS and TG-FTIR analyses

A Thermo Mass Photo TG-DTA-PIMS 410/S (Rigaku Corporation, Tokyo, Japan) was utilized to perform TG-MS analyses. Electron bombardment ionization source (EI) was chosen since EI ion source can be retrieved through the NIST library, and the structure and name of the analyte can be obtained. It was heated to 1000 °C at 20 °C/min in the 80% He/20% O<sub>2</sub> atmosphere, with the total gas flow rate of 300 mL/min to measure the intensity of some common gases. The initial temperature of the furnace in the synchronous thermal analysis was set to room temperature and continued for 60 min after the sample was sent to the furnace.

A TG (TG209 F1, NETZSCH, Germany)-FTIR (iS50 FT-IR, Thermo, America) system was used to analyze the combustion products of PA and PB. Transfer line and gas chamber were maintained at 260 °C to prevent the condensation. The air atmosphere was used as a reagent gas, while the purge gas intake of O<sub>2</sub> was set to 12 mL/min. The flow of N<sub>2</sub> gas was 45 mL/min to satisfy the air atmosphere ratio of 79% N<sub>2</sub>/21% O<sub>2</sub> with the total gas flow rate of 57 mL/min. All the samples were weighed to the same weight of  $10.0 \pm 0.5$  mg and heated from 25 to 1000 °C at 20 °C/min. A blank experiment was performed each time that the sample was loaded in order to eliminate the background signal interference.

### 2.4. Combustion performance indices

Based on the obtained TG data, burnout temperature ( $T_b$ ), ignition temperature ( $T_i$ ), maximum mass loss rate ( $-R_p$ ), and average mass loss rate ( $-R_v$ ) were estimated. The following four indices of the combustion performance were derived from the above estimates: ignition ( $D_i$ ), burnout ( $D_b$ ), flammability ( $D$ ) and comprehensive flammability ( $S$ ) indices thus (Huang et al., 2019b):

$$C_b = \frac{-R_p}{\Delta t_{1/2} \times t_p \times t_b} \quad (1)$$

$$C_i = \frac{-R_p}{t_i \times t_p} \quad (2)$$

$$D = \frac{-R_p}{T_i^2} \quad (3)$$

$$S = \frac{(-R_p) \times (-R_v)}{T_i^2 \times T_b} \quad (4)$$

where  $t_b$  is burn-out time;  $t_i$  is ignition time;  $t_p$  is peak time, and  $\Delta t_{1/2}$  is the time interval of the half value of  $-R_p$ . The higher heating rate points to higher burnout ( $D_b$ ) and ignition ( $D_i$ ) indices, and thus, a better combustion performance.

**Table 1**  
Results of physiochemical analyses of PA and PB on an air-dried basis.

Sample	PA	PB
Photograph		
Ultimate analysis (wt. %)		
C	41.70	42.42
N	1.54	0.79
H	5.21	5.01
S	0.15	0.07
O	51.40	51.71
Proximate analysis (wt. %)		
M	9.35	10.43
V	58.51	49.52
A	14.21	13.76
FC	17.93	26.29
HHV (MJ/Kg)	16.60	16.34

O = 100% - C - H - N - S (Chen et al., 2017a); M: moisture; V: volatiles; A: ash; FC: fixed carbon = 100% - M - A - V (Liu et al., 2019).

## 2.5. Kinetic analyses

### 2.5.1. Iso-conversional methods

Ignoring the effect of temperature on  $E_a$ , the combustion reaction rate can be expressed according to the Arrhenius's law as follows (Sun et al., 2019):

$$\beta = \frac{dT}{dt} \quad (5)$$

Eq. (5) can be transformed thus:

$$\frac{d\alpha}{dT} = \frac{A}{\beta} e^{\left(\frac{-E_a}{RT}\right)} f(\alpha) \quad (6)$$

where conversion rate also known as normalization  $\alpha \in [0, 1]$  is shown below:

$$\alpha = \frac{(m_0 - m_t)}{(m_0 - m_f)} \quad (7)$$

where  $t$ ,  $\alpha$ , and  $f(\alpha)$  are time, conversion degree and unknown reaction mechanism, respectively.  $A$ ,  $E_a$ ,  $R$ , and  $T$  are the pre-factor, apparent activation energy, general gas constant, and absolute temperature, respectively.  $m_0$ ,  $m_t$ , and  $m_f$  refer to the initial, instantaneous and final masses of the samples, respectively.

The iso-conversional methods can be used to predict  $E_a$  at a given  $\alpha$  in a model-independent manner and to avoid errors due to the prior selection of a reaction mechanism (Zhang et al., 2019b). The Friedman method is one of the most common methods for the kinetic analysis of a single reaction and yields more accurate  $E_a$  estimates as follows (Hu et al., 2017):

$$\ln \beta \left( \frac{d\alpha}{dT} \right) = - \frac{E_a}{RT} + \ln(A \cdot f(\alpha)) \quad (8)$$

The Flynn-Wall-Ozawa (FWO) method derives  $E_a$  from the TG curve based on the temperature of a few integrated analytical plots with a constant weight loss at different heating rates as follows (Chen et al., 2015):

$$\ln \beta = \ln \left( \frac{AE_a}{Rg(\alpha)} \right) - 5.3305 - 1.052 \left( \frac{E_a}{RT} \right) \quad (9)$$

where  $g(\alpha)$  represents the integrated form of the reaction function. Distributed activation energy method (DAEM) is a common

multi-reaction model whose distribution function of  $E_a$  is based on the simultaneous occurrence of innumerable reactions during the biomass combustion (Jain et al., 2016). In this model, the relationship between the temperature and heating rate is expressed thus:

$$\ln \left( \frac{\beta}{T^2} \right) = \ln \left( \frac{AR}{E_a} \right) + 0.6075 - \frac{E_a}{RT} \quad (10)$$

The Starink method is used to estimate  $E_a$  as follows (Chen et al., 2017c):

$$\ln \left( \frac{\beta}{T^{1.92}} \right) = C_s - 1.0008 \left( \frac{E_a}{RT} \right) \quad (11)$$

### 2.5.2. Integral master-plots (IMP) method

The integral of Eq. (6) can be obtained thus (Huang et al., 2019b):

$$g(\alpha) = \int_0^\alpha \frac{d\alpha}{f(\alpha)} = \frac{A}{\beta} \int_{T_0}^T e^{\left(\frac{-E_a}{RT}\right)} dT = \frac{AE_a}{\beta R} [P(u) - P(u_0)] \quad (12)$$

where  $P(u)$  represents temperature integral; and  $u = \frac{E_a}{RT}$ . Thus, Eq. (12) can be re-arranged as follows (Liu et al., 2016):

$$g(\alpha) = \frac{AE_a}{\beta R} P(u) \quad (13)$$

$$P(u) = \frac{e^{(-u)}}{u \times (1.0019882u + 1.87391198)} \quad (14)$$

$E_a$  was estimated using the FWO method to find the most appropriate reflection function. Adopting  $\alpha = 0.5$  and  $u = 0.5$  as the reference value, the below equation was obtained (Cai et al., 2019):

$$g(0.5) = \frac{AE_a}{\beta R} P(0.5) \quad (15)$$

where  $g(0.5)$  is the integral function at  $u = 0.5$ ;  $u_{0.5} = \frac{E_a}{RT_{0.5}}$  is the temperature at  $u = 0.5$ . From the above equations, the formula of the IMP method was derived thus (Chen et al., 2017b):

$$\frac{g(x)}{g(0.5)} = \frac{P(u)}{P(u_{0.5})} \quad (16)$$

The most common reaction models for the solid thermal decomposition are listed in Table 2.

2.6. Statistical analyses

The four responses of DTG (%/min), DSC (mW/mg), RM (%), and conversion rate (α) were jointly optimized considering composite desirability (D) in response to the four predictors of time (min), temperature (°C), heating rate (°C/min), and *P. vittata* residue type. Composite desirability as a geometrical average of individual desirability (d) varies between 0 and 1 (the ideal condition). The ordinal and nominal predictors of heating rate, and *P. vittata* residue type had the four levels of 5, 10, 20 and 40 °C/min and the two levels of (1) PA and (2) PB, respectively. The joint optimization was based on the best-fit multiple non-linear regression (MNL) models chosen through a stepwise procedure, and the decision rule of p-value of 0.001 to retain the predictors in the model. All the statistical analyses were performed using Minitab 17.1.

3. Results and discussion

3.1. Emission analysis

Although they are the parts of the same plant, PA and PB had a different performance of emission levels from their combustions (Fig. 1a–b). The emitted gases consisted of the following two categories: (1) gases with potential energy utilization (H<sub>2</sub>, CH<sub>4</sub>, CO<sub>2</sub>, and NH<sub>3</sub>), and (2) other gases (CO, NO, NO<sub>2</sub>, SO<sub>2</sub> and HCN) detected in the MS phase (Fig. 2a–c). The relative yield of the gas products was estimated using the integration of the MS curve in Fig. 2c. Table 4 shows the releases of the two types of gases as a function of temperature. The releases of these gases were exothermic, as indicated by the arrows in Figs.

According to the wavelength ranges corresponding to the various functional groups as shown in the Supplementary Materials (Table S1), various gaseous products can be analyzed more accurately. Since not only N<sub>2</sub> and CO but also CO<sub>2</sub> and N<sub>2</sub>O have the same molecular weights of 28 and 44, respectively, TG-MS analyses need

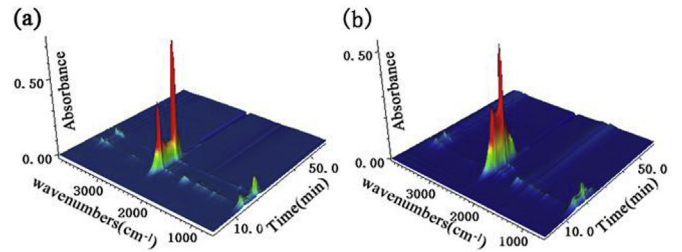


Fig. 1. 3-D infrared characterization of emissions at 20 °C/min from (a) PA and (b) PB combustions.

to be combined with TG-FTIR analyses (Fig. 1a–b) to determine the type of gases. In addition to the appearance of 10 gaseous peaks according to TG-FTIR analyses, there were some organic by-products of the thermal degradation. Most of the gases were quickly released from the PA combustion in the ranges of 200–400 °C and 400–500 °C (Fig. 1a). However, the gas evolution of the PB combustion had a wider temperature range of 130–700 °C (Fig. 1b). The releases of H<sub>2</sub>O were mainly from the crystal water by H–O–H bending of the biomass, or the reaction of oxygen functional groups by O–H stretch (Liang et al., 2018). The functional groups of O–H stretch between 1820 and 1660 cm<sup>-1</sup> and –C–H bending between 1500 and 1300 cm<sup>-1</sup> were attributed to the fact that PA and PB were rich in acid and hydrocarbon. The functional groups of –C–H stretch in the range of 3115 to 2675 cm<sup>-1</sup> and C–O stretch in the range of 1300 to 950 cm<sup>-1</sup> were linked to the existence of aldehydes/ketones, and ethers/alcohols/phenols, respectively. It should be noted that TG-FTIR analyses can describe the type of functional groups, but the gaseous products cannot be quantitatively analyzed. Therefore, for the gas evolutions to be comprehensively detected, TG-MS analyses were indispensable.

The main emissions were related to the carbonaceous (Fig. 2c) (PA: 90.50%; PB: 90.80%) and N-containing species (PA: 6.95%; PB: 6.56%). Both PA and PB combustions showed a significant advantage in terms of CO<sub>2</sub> (PA: 54.53%; PB: 54.36%) and NH<sub>3</sub> emissions (PA: 60.58%; PB: 60.65%) (Fig. 2c). *Pteris vittata* is a CO<sub>2</sub>-neutral fuel

Table 2 Common functions of reaction mechanism based on FWO (Hu et al., 2019).

Symbol	Reaction mechanism	$f(\alpha) = \frac{(1/k)}{(d\alpha/dt)}$	$g(\alpha) = kt$
<b>Nucleation models</b>			
A1.5	Avarami-Erofeev	$1.5(1-\alpha)[-ln(1-\alpha)]^{1/3}$	$[-ln(1-\alpha)]^{2/3}$
A2	Avarami-Erofeev	$2(1-\alpha)[-ln(1-\alpha)]^{1/2}$	$[-ln(1-\alpha)]^{1/2}$
A3	Avarami-Erofeev	$3(1-\alpha)[-ln(1-\alpha)]^{2/3}$	$[-ln(1-\alpha)]^{1/3}$
An	Avarami-Erofeev	$n(1-\alpha)[-ln(1-\alpha)]^{(n-1)/n}$	$[-ln(1-\alpha)]^{1/n}$
<b>Diffusion models</b>			
D1	One-dimension diffusion	$1/(2\alpha)$	$\alpha^2$
D2	Valensi	$[-ln(1-\alpha)]^{-1}$	$(1-\alpha)ln(1-\alpha)+\alpha$
D3	Jander	$[(3/2)(1-\alpha)^{2/3}]/[1-(1-\alpha)^{1/3}]$	$[1-(1-\alpha)^{1/3}]^2$
D4	Ginstling-Brounshtein	$[(3/2)(1-\alpha)^{1/3}]/[1-(1-\alpha)^{1/3}]$	$(1-2\alpha/3)-(1-\alpha)^{2/3}$
<b>Reaction order models</b>			
F1	First order reaction	$1-\alpha$	$-ln(1-\alpha)$
F2	Second order reaction	$(1-\alpha)^2$	$(1-\alpha)^{-1}-1$
F3	Third order reaction	$(1-\alpha)^3$	$[(1-\alpha)^{-2}-1]/2$
Fn	nth order reaction	$(1-\alpha)^n$	$[(1-\alpha)^{(1-n)}-1]/(n-1)$
<b>Geometrical contraction models</b>			
G2	Contracting cylinder	$2(1-\alpha)^{1/2}$	$1-(1-\alpha)^{1/2}$
G3	Contracting sphere	$3(1-\alpha)^{1/3}$	$1-(1-\alpha)^{1/3}$
<b>Power law models</b>			
P2	2-Power law	$2\alpha^{1/2}$	$\alpha^{1/2}$
P3	3-Power law	$3\alpha^{1/3}$	$\alpha^{1/3}$
P4	4-Power law	$4\alpha^{1/4}$	$\alpha^{1/4}$

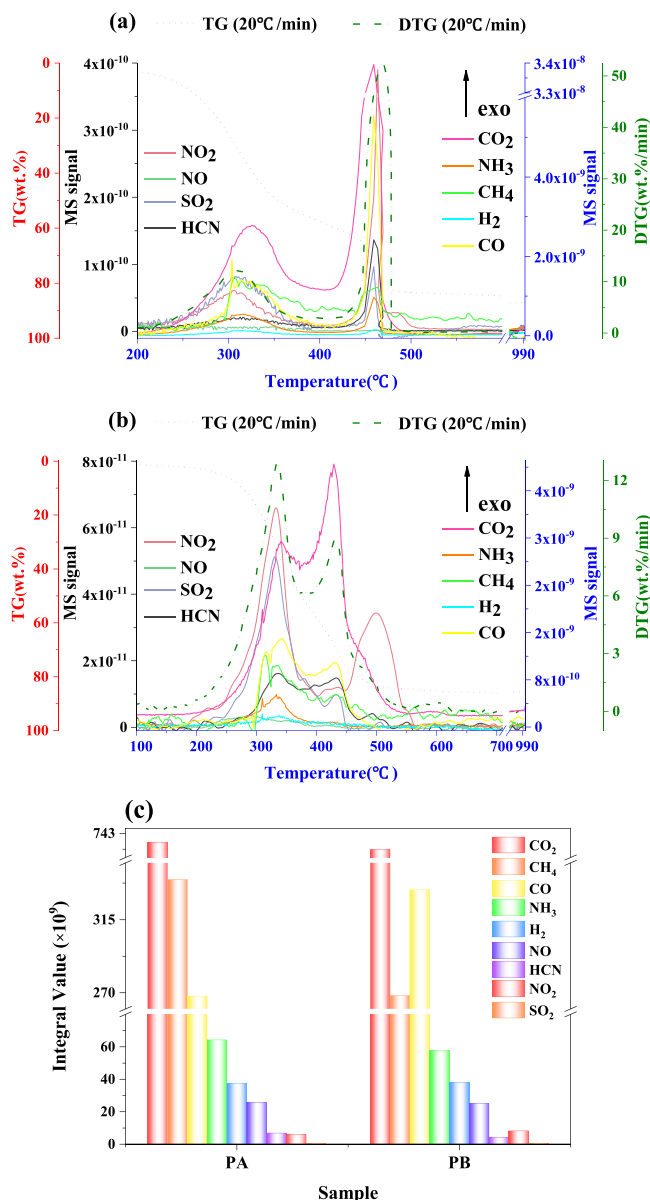


**Fig. 2.** Conversion degrees, DTG curves, and MS signals of emissions from (a) PA and (b) PB combustions at 20 °C/min up to 1000 °C in the air atmosphere, and (c) the integral value of each gas (arrow indicates the exothermic directions).

by which the amount of CO<sub>2</sub> emission to the atmosphere from its combustion is equal to the amount of CO<sub>2</sub> sequestration from the atmosphere via photosynthesis (Darda et al., 2019). Carboxyl (C = O) in macromolecular organics was broken at higher temperatures, producing a large amount of CO<sub>2</sub>. CH<sub>4</sub> was released mainly at below 400 °C and between 350 and 500 °C. This was probably due to the secondary decomposition of organic compounds such as ketones, alcohols, aldehydes, and acids, thus leading to chain scission and reforming reactions (Tian et al., 2014). The thermal instability of carbonyl (R-O-R) (Fang et al., 2017) and C=O generated CO at low temperatures (Xie et al., 2018). For both, the second peak of CO<sub>2</sub> emission was more prominent than the first peak in Fig. 3a–b since CH<sub>4</sub> and CO continued to be oxidized as CO<sub>2</sub>. Though being found in the range of 250–480 °C, H<sub>2</sub> eventually reacted with oxygen to form water and disappeared. CO<sub>2</sub> emission was positively

correlated with the C content of the combusted samples, whereas SO<sub>2</sub> and NO<sub>x</sub> emissions were not necessarily related to their N and S contents. The relatively low conversion rate of PA, and its relatively high N and S contents suggested that N and S were in the form of reductive intermediates.

Since biomass contains a large amount of amino groups, the nitrogenous volatiles following their initial combustion were reported to generally generate NH<sub>3</sub> (Mladenović et al., 2018). Not only did NH<sub>3</sub> lead to a very low flame speed, combustion instability, and ignition difficulty but also to a high NO<sub>x</sub> emission level (Mosevitzky et al., 2018). HCN appeared to be produced by the degradation of intermediate heterocyclic-N compounds at low temperatures (Huang et al., 2019a). Both NH<sub>3</sub> and HCN were ultimately converted to NO and its derivatives by a series of oxidation reactions (Wang et al., 2019b). This was consistent with the temperature range of the emissions shown in Table 3. The proportion of the released gas pollutants was more from the PB than PA combustion. For example, 172.44% SO<sub>2</sub>, 137.49% NO<sub>2</sub> and 124.48% CO were released more from the PB than PA combustion. Most of the air pollutants were produced at below 500 °C for PA and below 700 °C for PB. The present study provides a reference to guide the pollution control in practice. SO<sub>2</sub> emissions from the PA and PB combustions can be controlled using the conventional approaches for the coal combustion such as fluidized bed combustion, calcium spray in the furnace, and flue gas desulfurization. NO<sub>x</sub> emission reductions can be achieved using fuel-staged combustion, flue gas recirculation, and flue gas denitrification such as selective (non-)catalytic reductions. Temperature was the driving variable behind the fate of NO<sub>x</sub> emission from the combustion (Shah et al., 2018). Therefore, the PB combustion needs more controls over its emissions than does the PA combustion. It is also necessary to set a higher temperature for PB to be burnt to reduce its emissions. This is the simplest and most effective method for a cleaner production, but how to increase the temperature, and how to burn the fuels still remain to be analyzed in the following sections for the combustion behavior and dynamics.

### 3.2. Thermogravimetric analysis

According to the DTG curve at 20 °C/min, PA (Fig. 4a) had three peaks, while PB (Fig. 4b) had one more peak at 500 °C. Their combustion process consisted of the following four stages (Table 4): (1) moisture evaporation; (2) combustion of volatiles; (3) combustion of fixed carbon and some volatiles; and (4) degradation of inorganic materials and residues (Zhang et al., 2019a). With the increased temperature, PA was dried faster than PB. The narrower  $T_{P1}$  range of PA than PB indicated the better water retention ability of PB than PA. The second stage was the combustion stage of plant organic matter such as hemicellulose, cellulose, and lignin whose decomposition generated volatiles and carbon (Dhyani and Bhaskar, 2018). At this stage, the TG curve of PA dropped sharply accounting for 59.06% of the total weight loss. The earlier weight loss peak ( $T_{P2}$ ) of PA than PB with a 20 °C lower peak temperature and a 2.04%/min higher peak rate showed that the low boiling-point compound and hemicellulose contents of PA were higher than those of PB (Huang et al., 2018). The third stage belonged to the combustion of fixed carbon and volatiles with strong chemical bonds such as macromolecular compounds (Wang et al., 2018b). PA underwent the third weight loss stage (28.29%), accounting for 32.67% of the total weight loss. The narrower DTG peak ( $T_{P3}$ ) range of the char combustion of PA than PB, with a 20 °C higher  $T_{P3}$  and a higher heating rate indicated that PA was burnt faster and caught fire earlier. Also, the fourth weight losses of 1.71% and 1.65% by PA and PB, respectively, were evidenced by the existence of some alkali

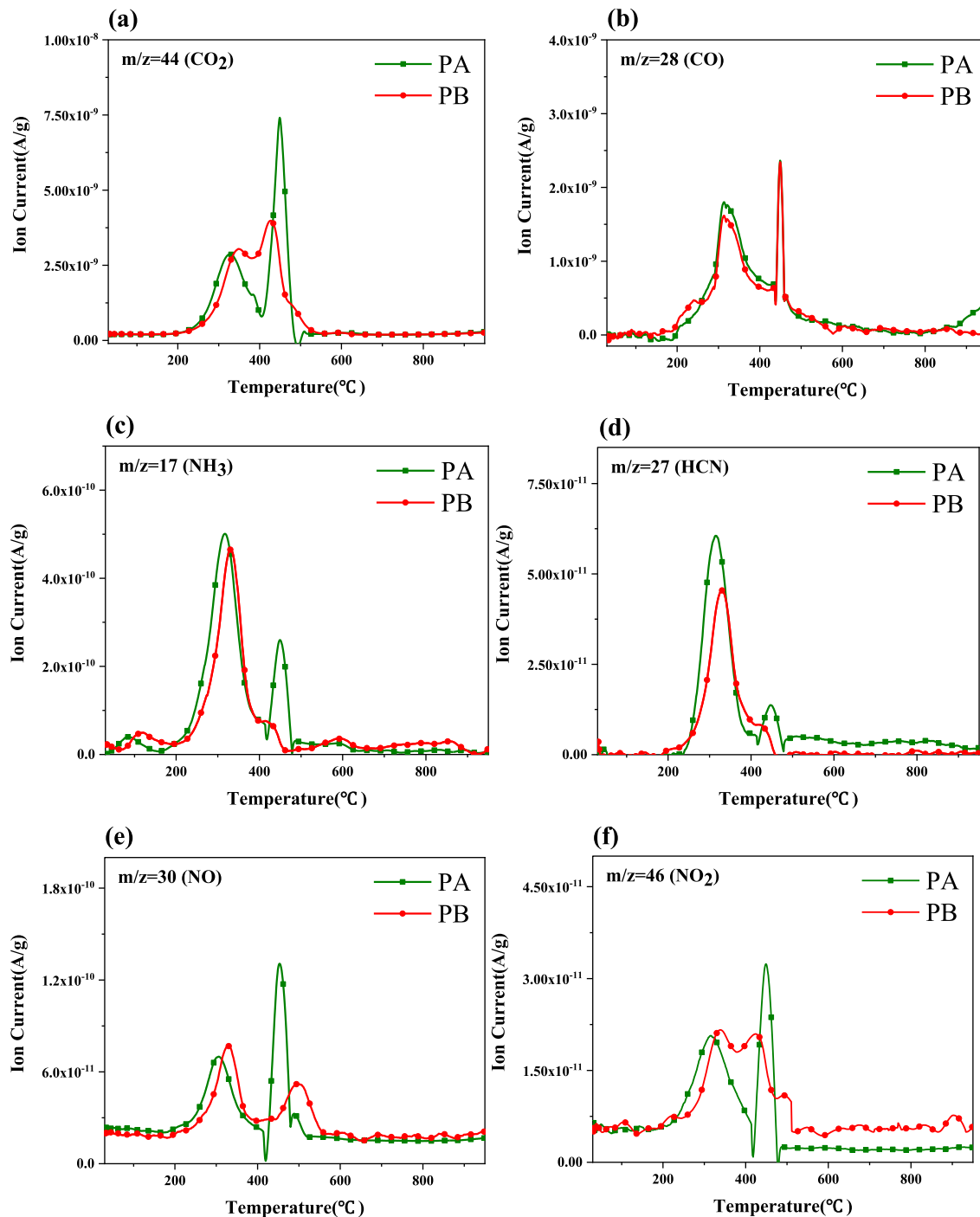


Fig. 3. MS curves of common ions during the PA and PB combustions at 20 °C/min.

metals such as Na, K, and Ca decomposed in the high temperature region.

The DTG curves of both biomass parts showed three similar peaks with the second peak having the largest mass loss (Fig. 5b and d). With the elevated heating rate, the DTG curves had a similar pattern of moving to the high temperature regions of PA (Fig. 5b) and PB (Fig. 5d), also known as thermal hysteresis (Cai et al., 2018). The decomposition mode of PB did not change significantly. However, the maximum peak of PA at the low heating rates (5 and 10 °C/

min) occurred with  $T_{p3}$ , while its maximum peak at the high heating rates (20 and 40 °C/min) occurred with  $T_{p2}$ . This may be because the hemicellulose combustions of PA and PB had the lowest activation energy, as can be seen in Section 3.5. Hemicellulose and cellulose were decomposed slowly at the low heating rates, thus resulting in the partial carbonization and combustion of char in the third stage (Huang et al., 2016). The PA and PB masses almost remained constant at above 650 °C and 510 °C, respectively, indicating the reaction stability. Therefore, the increased heating

**Table 3**  
Peak temperatures of various gas pollutants released from PA and PB combustions.

Samples	Gas	PA			PB		
		Range (°C)	Peak 1 (°C)	Peak 2 (°C)	Range (°C)	Peak 1 (°C)	Peak 2 (°C)
gases with potential energy utilization	CO <sub>2</sub>	180–500	326	462	160–700	353	425
	NH <sub>3</sub>	70–500	317	459	60–490	331	428
	CH <sub>4</sub>	270–490	305	460	280–500	323	432
	CO	240–480	304	458	300–490	342	431
	H <sub>2</sub>	250–470	315	459	250–480	337	NP
Other gases	NO <sub>2</sub>	130–500	310	450	100–650	339	426
	NO	150–450	305	451	180–600	335	501
	SO <sub>2</sub>	160–460	305	NP	180–490	325	NP
	HCN	230–500	309	450	180–490	329	424

NP: no peak.

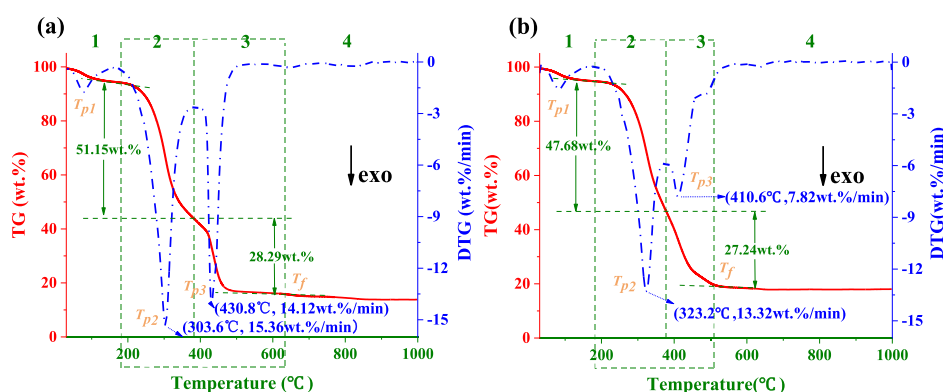


**Fig. 4.** (D)TG curves of (a) PA and (b) PB combustions at 20 °C/min (arrow indicates the exothermic directions).

**Table 4**  
Mass losses of PA and PB as a function of temperature at 20 °C/min.

	Stage	Temperature range (°C)	Mass loss (wt %)	Max mass loss rate (wt %/min)	Percentage (%)	Total mass loss (wt %)
PA	1	<182	5.45	1.76	6.29	86.60
	2	182–382	51.15	15.36	59.06	
	3	382–653	28.29	14.12	32.67	
	4	653–999	1.71	–	1.97	
PB	1	<182	5.30	1.59	6.47	81.87
	2	182–375	47.68	13.32	58.24	
	3	375–509	27.24	7.82	33.27	
	4	509–998	1.65	–	2.02	

rate was conducive to the volatilization and burning of volatiles but to burnout.

### 3.3. Combustion characteristics

Table 5 gives the 14 combustion characteristics. The elevated heating rate delayed the decomposition process and affected the characteristic temperatures ( $T_i$  and  $T_b$ ), times ( $t_i$ ,  $t_b$ , and  $\Delta t_{1/2}$ ) and mass loss rates ( $-R_p$  and  $-R_v$ ). The elevated heating rate significantly increased the  $T_b$ ,  $T_i$  and  $T_p$  values of PA and PB (Guo and Zhong, 2018).  $T_b$  of the samples varied significantly depending on their fixed carbon and ash contents since the combustion of hemicellulose formed a gray shell coating on the lignin surface, thus hindering the penetration of oxygen and the outward diffusion of the combustion products (Liang et al., 2018).

The higher the heating rate was, the faster the reaction rate was, and the shorter the burn-up time was (Tian et al., 2014). The

increased  $-R_p$  and  $-R_v$  values of PA and PB resulted from the increased heat energy supply from the inside and outside of the particles, and the enhanced heat transfer ability between the particles.  $C_b$ ,  $C_i$ ,  $D$ , and  $S$  also rose with the elevated heating rate (Table 5). The burn-up performance ( $C_b$ ) of PA was superior to that of PB. The combustion characteristic index ( $S$ ) of PA was less than that of PB at the low heating rates; however, the opposite was true at the high heating rates (see Section 3.2 for explanation). The  $C_i$  values of PA and PB were higher than those of sludge ( $4.23 \times 10^{-2}\%/\text{min}^3$ ), and pulverized coal ( $4.69 \times 10^{-2}\%/\text{min}^3$ ) (Huang et al., 2018). PA not only had a short ignition time but also a short burning time which pointed to its high combustion efficiency.

### 3.4. DSC and DDSC analyses and joint optimization

DSC analysis is a measure of the energy difference between an input (sample) and a reference over temperature or time (He et al.,

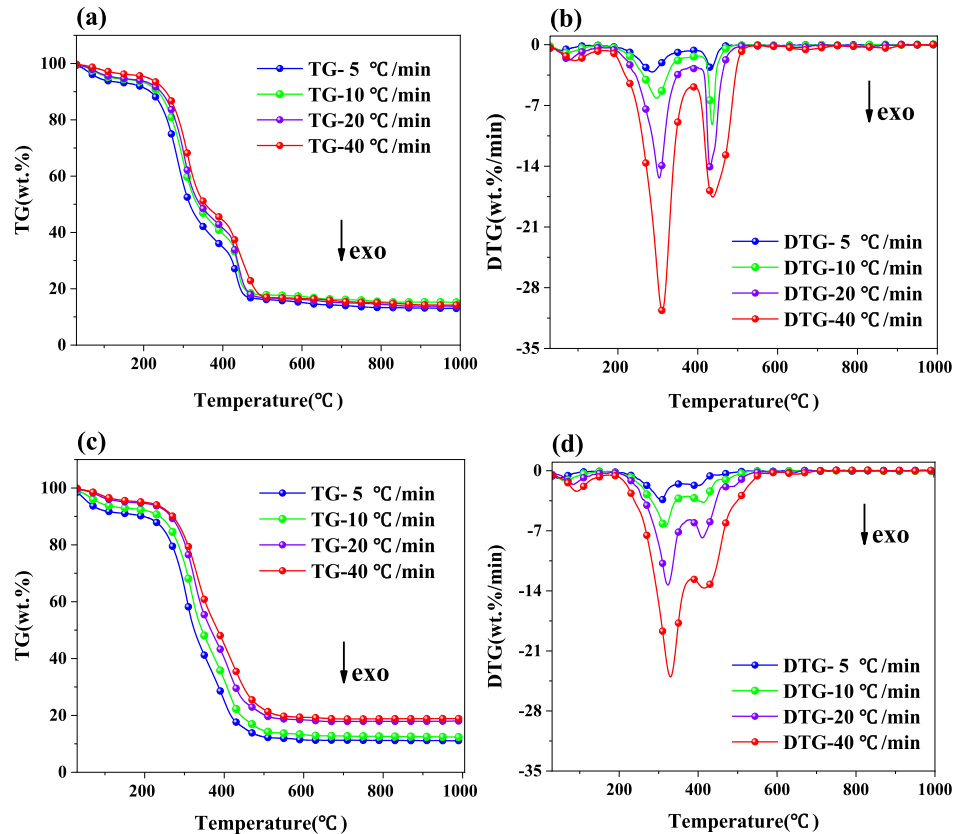


Fig. 5. TG curves of (a) PA and (c) PB combustions, and DTG curves of (b) PA and (d) PB combustions at four heating rates (arrow indicates the exothermic directions).

Table 5

14 combustion characteristic parameters of PA and PB in response to four heating rates based on TG experiments in the air atmosphere.

Sample	PA				PB			
	5	10	20	40	5	10	20	40
$\beta$ ( $^{\circ}\text{C}/\text{min}$ )	5	10	20	40	5	10	20	40
$-R_p$	3.14	6.16	15.36	30.67	3.44	6.54	13.32	24.02
$-R_v$	0.45	0.91	1.89	4.00	0.46	0.91	1.76	3.69
$M_r$	12.99	15.20	13.83	14.23	11.08	12.33	18.02	18.88
Temperature ( $^{\circ}\text{C}$ )								
$T_b$	622	624	653	670	489	517	510	524
$T_i$	251	259	272	276	272	260	290	289
$T_p$	286	297	304	311	307	316	323	330
Time (min)								
$\Delta t_{1/2}$	47.65	24.78	13.25	7.15	51.37	27.42	14.20	7.88
$t_b$	90.50	46.60	24.80	13.10	95.90	53.30	28.90	15.92
$t_i$	44.42	23.10	12.65	6.85	48.58	23.23	13.48	7.08
$t_p$	51.90	40.60	20.00	7.50	57.20	38.70	19.50	10.20
Combustion characteristic indices								
$C_b$	0.001	0.013	0.234	4.366	0.001	0.012	0.166	1.880
$C_i$	0.14	0.66	6.07	59.70	0.12	0.73	5.07	33.26
$D$	0.50	0.92	2.07	4.03	0.47	0.97	1.58	2.87
$S$	0.36	1.33	6.00	24.09	0.44	1.70	5.46	20.24

2006). The DSC curves of the PA (Fig. 6a) and PB (Fig. 6c) combustions exhibited clearly different shapes and stages from those of the traditional coal fuels (Shi et al., 2018). This may be because bituminous coal and anthracite contained more fixed carbon and less volatiles matter, while biomass had more volatiles matter and less fixed carbon. Overall, lignite had more volatiles matter, but not more than did biomass (Zhang et al., 2018). Both PA and PB involved exothermic reactions. The arrows in the TG-DTG-DSC curves

indicated their exothermic directions. The DSC curves of PA and PB had very prominent exothermic peaks in both flammable and flame-retardant parts and were consistent with the conclusions drawn in Section 3.1. For PA and PB, the exothermic peaks moved to the higher temperature zones with the higher heating rate (Wang et al., 2015).

DDSC is a differential form of DSC that reflects the rates of change in chemical reactions (Zhuo et al., 2017). When PA and PB were burnt reaching  $T_i$  or  $T_b$ , the heat release rates peaked, corresponding to the zero points of the DDSC curve (the inflection point of the DSC) or the extreme points in the DDSC curve (He et al., 2006). The effect of the heating rate on the PA and PB combustions can be seen in Fig. 6b and d. The increased absolute heat flow rate with the increased heating rate indicated that the heating rate enhanced the exothermic behavior (Huang et al., 2018).

The best-fit MNL models obtained in this study accounted for 99.62, 99.61, 97.96 and 84.64% of variations in RM,  $\alpha$ , DSC, and DTG, respectively (see online Supplementary Materials). The joint optimization was based on the above MNL models with the objective functions of the maximization of  $\alpha$ , DTG, and DSC, and the minimization of RM. The 10 best solutions of the joint optimization pointed to 999.2 and 514.6  $^{\circ}\text{C}$ , 193.6 and 97.1 min, and 40  $^{\circ}\text{C}/\text{min}$  for PB and PA, respectively, as the optimum operational conditions with the same D value of unity (Fig. 7). The second optimum settings were determined as 515  $^{\circ}\text{C}$ , 97.1 min, 5  $^{\circ}\text{C}/\text{min}$ , and PA ( $D=0.60$ ). Sensitivity analyses showed that the heating rate exerted a significant impact on the joint optimization, while the selection of PA versus PB did not significantly affect the optimization parameters. Overall, the cleanest production schemes were 999.2

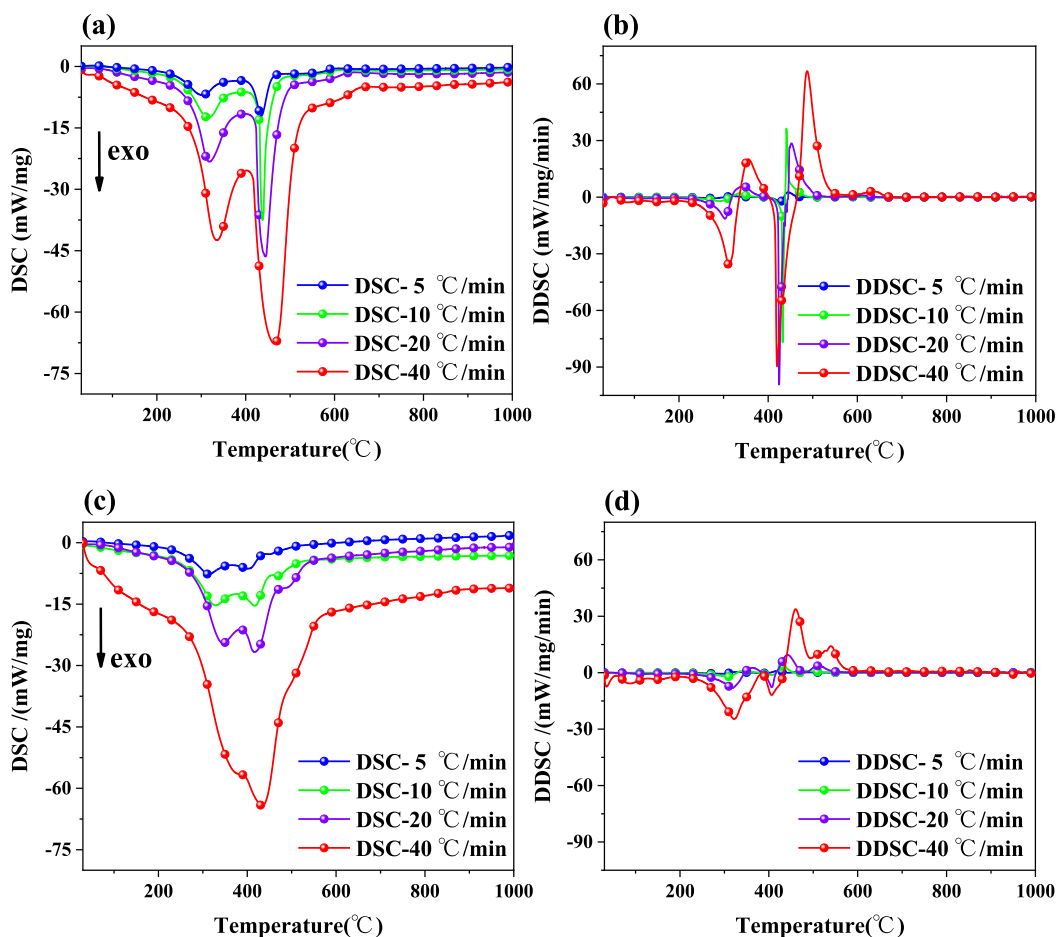


Fig. 6. DSC analyses of (a) PA and (c) PB combustions and DDSC analyses of (b) PA and (d) PB combustions at four heating rates (arrow indicates the exothermic directions).

and 514.6 °C, 193.6 and 97.1 min, and 40 °C/min for PB and PA, respectively. These settings achieved the maximized heat release as well as the minimized emissions. PA appeared to enable the most efficient combustion in the industrial-scale reactors or incinerators. These results contribute to developing the new strategies for a cleaner production with the *P. vittata* combustion.

### 3.5. Kinetic analyses

Hemicellulose was most susceptible to the thermal exothermic degradation in the range of 220–315 °C. The cellulose decomposition was an endothermic reaction in the range of 314–400 °C, while the exothermic reaction of lignin occurred between 160 and 900 °C (Yang et al., 2007). Since the second and third stages were the main stages of weight losses of PA and PB (Table 4), they accounted for 91.73% and 91.51% of the total losses, respectively, corresponding to the conversion degree range of 0.05–0.98. To avoid the interference of moisture in the low temperature and its reactions in the high temperature, the conversion degree range of 0.1–0.9 was selected and divided into three sub-stages (Table 6). In other words, based on the Fraser–Suzuki deconvolution in the Origin 9 software, the entire combustion process of *P. vittata* (150 °C–1000 °C) at 20 °C/min was divided into the three pseudo-component single reactions of pseudo-hemicellulose (PA: 150–300 °C; PB: 150–292 °C), pseudo-cellulose (PA: 300–400 °C; PB: 292–360 °C), and pseudo-lignin + char (PA: 400–465 °C; PB: 360–475 °C).

The  $E_a$  estimates based on the FWO, DAEM and Starink methods were similar during the entire combustion processes see online Supplementary Materials (Table S2). The lower  $R^2$  values (0.8–0.9) for the  $E_a$  estimates by the Friedman method at  $\alpha = 0.5$  or between 0.7 and 0.9 may be due to the lack of the involvement of a mathematical approximation. Thus, it was subjected to errors caused by the fluctuations of the TG curve (Cai et al., 2018). The FWO method was chosen to calculate the suitable mechanism model at 20 °C/min. Fig. 8c–d shows the combustion mechanisms of the three stages. Overall, the ranges of  $E_a$  were lower and narrower for PB than PA for the three single sub-reactions (Fig. 8a–b).

The mean  $E_0$  value of the pseudo-hemicellulose reaction ( $\alpha_1 = 0.1–0.357$ ) for PA was estimated at 188.60 kJ/mol, corresponding to the D4 Ginstling-Brounshtein diffusion model ( $R^2 = 0.9988$ ). The mean  $E_0$  value of the pseudo-hemicellulose reaction ( $\alpha_1 = 0.1–0.194$ ) for PB was estimated at 135.96 kJ/mol, corresponding to the D1 one-dimension diffusion model ( $R^2 = 0.9997$ ). In the pseudo-cellulose stage, the mean  $E_0$  value of PA ( $\alpha_2 = 0.357–0.676$ ) was 214.31 kJ/mol, corresponding to F3 order reaction ( $R^2 = 0.9960$ ), while that of PB ( $E_0 = 167.46$  kJ/mol;  $\alpha_2 = 0.194–0.582$ ) pointed to in between F1 and F1.5 ( $R^2 = 0.9997$ ). After several iterations, F1.3 order reaction was determined as the most suitable model. The mechanism model for cellulose was in close agreement with the results by (Liu et al., 2016).

In the last stage (pseudo-lignin + char), both PA and PB belonged to the reaction order models with the different levels. The

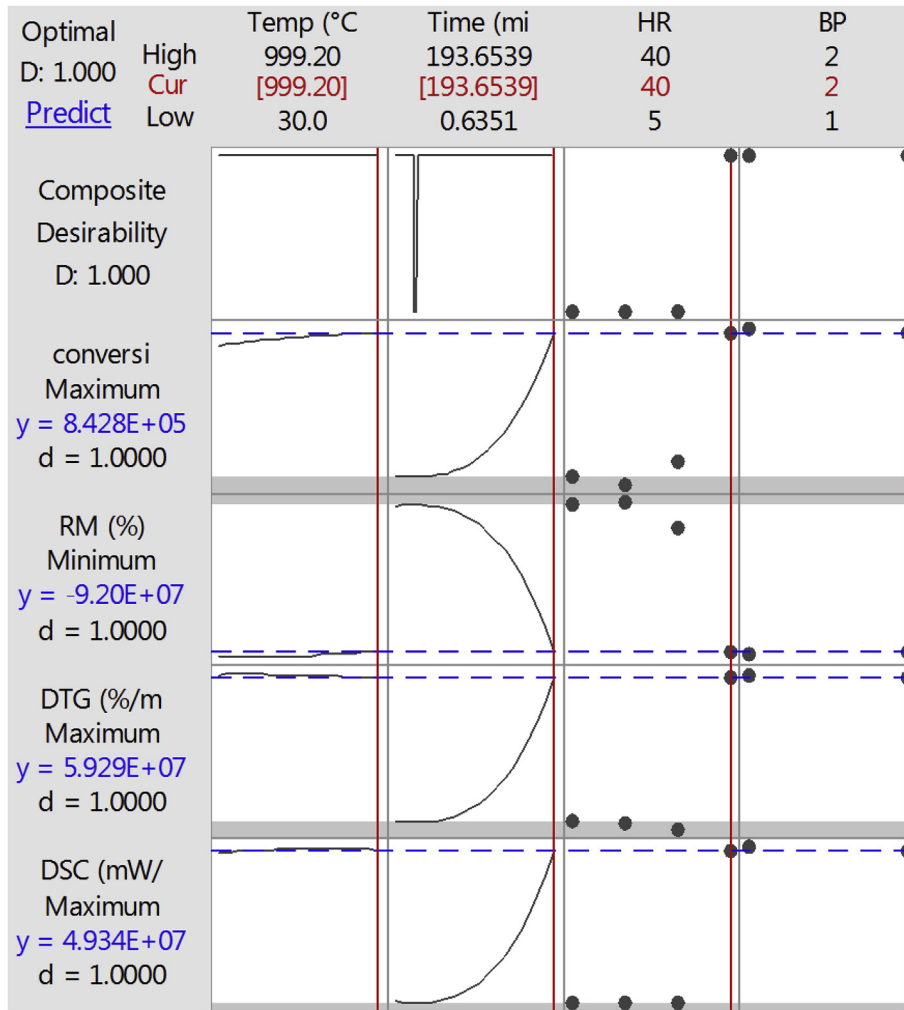
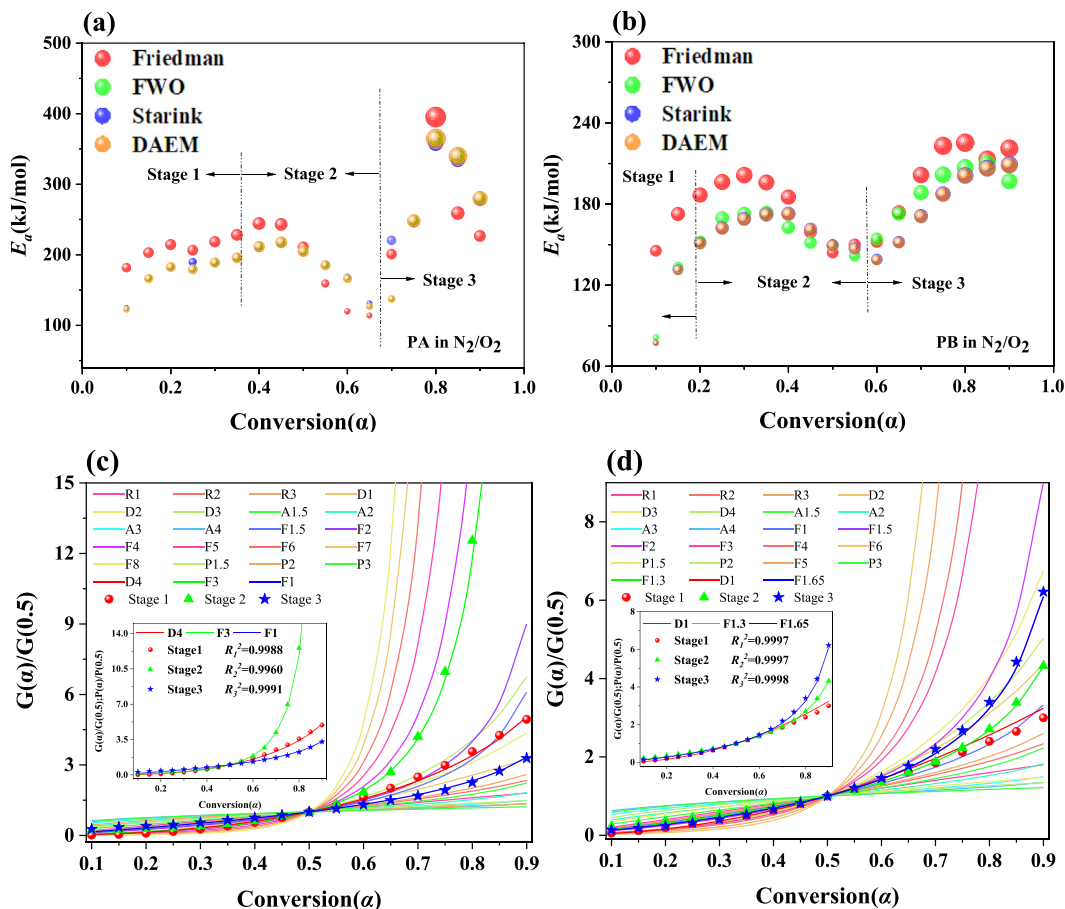


Fig. 7. Joint optimization of  $\alpha$ , RM, DTG, and DSC in response to time, temperature, heating rate, and aboveground (PA) and belowground (PB) biomass of *Pteris vittata* (The vertical solid red lines denote the optimum settings, while the horizontal dashed blue lines indicate fitted values of the response). (For interpretation of the references to colour in this figure legend, the reader is referred to the Web version of this article.)

Table 6  
 $E_a$  (kJ/mol) estimates of PA and PB combustions according to FWO at 20 °C/min as a function of conversion degree ( $\alpha$ ), and reaction stage.

$\alpha$	PA						PB					
	Stage 1		Stage 2		Stage 3		Stage 1		Stage 2		Stage 3	
	$E_a$ (kJ/mol)	$R^2$										
0.10	184.96	0.9510	204.56	0.9843	123.90	0.9838	109.12	0.8629	159.55	0.9685	152.01	0.9879
0.15	193.04	0.9822	208.20	0.9830	136.88	0.9616	117.15	0.8901	162.55	0.9738	154.80	0.9864
0.20	188.07	0.9875	210.90	0.9798	169.26	0.9042	130.42	0.8674	140.23	0.9083	156.69	0.9869
0.25	187.47	0.9866	216.03	0.9772	205.06	0.9035	131.84	0.8577	183.01	0.8843	159.86	0.9836
0.30	184.67	0.9927	235.89	0.9894	249.95	0.8842	130.84	0.8846	170.00	0.9784	163.43	0.9830
0.35	186.27	0.9929	251.19	0.9902	308.91	0.8999	138.45	0.9172	172.30	0.9812	168.56	0.9808
0.40	187.51	0.9931	248.76	0.9904	340.88	0.9042	139.08	0.9310	174.48	0.9823	172.79	0.9795
0.45	189.62	0.9947	248.87	0.9937	366.68	0.9337	138.79	0.9408	175.44	0.9824	179.87	0.9791
0.50	191.44	0.9940	244.78	0.9950	372.39	0.9482	142.47	0.9363	176.00	0.9855	185.41	0.9811
0.55	189.00	0.9946	243.12	0.9962	356.72	0.9424	142.01	0.9411	176.80	0.9866	188.67	0.9790
0.60	189.55	0.9938	230.43	0.9987	339.37	0.9284	140.78	0.9381	175.51	0.9887	192.48	0.9782
0.65	187.96	0.9932	217.53	0.9997	320.07	0.9124	140.99	0.9445	172.51	0.9906	194.86	0.9779
0.70	186.69	0.9928	205.11	0.9997	297.30	0.8915	140.88	0.9459	170.48	0.9905	197.50	0.9810
0.75	190.00	0.9924	189.45	0.9991	275.94	0.8692	141.95	0.9482	165.43	0.9925	196.65	0.9797
0.80	189.05	0.9922	170.65	0.9981	263.20	0.8596	142.99	0.9492	161.70	0.9926	198.43	0.9846
0.85	190.24	0.9906	154.60	0.9967	252.79	0.8514	143.11	0.9537	157.16	0.9927	197.06	0.9808
0.90	190.67	0.9899	163.14	0.9612	247.96	0.8593	140.37	0.9513	153.60	0.9919	182.26	0.8282
Average	188.60	0.9891	214.31	0.9901	272.19	0.9081	135.96	0.9212	167.46	0.9748	178.90	0.9728



**Fig. 8.** Comparisons of apparent activation energy versus conversion degree by three model-free results for (a) PA and (b) PB combustions; and comparisons of three experimental stages and theoretical mechanisms of (c) PA and (d) PB combustions by IMP based on FWO estimates.

mean  $E_0$  value of 272.19 kJ/mol for PA ( $\alpha_3 = 0.676-0.9$ ) corresponded to F1 order reaction ( $R^2 = 0.9991$ ). The mean  $E_0$  value of 178.90 kJ/mol for PB ( $\alpha_3 = 0.582-0.9$ ) was in between F1.5 and F2 ( $R^2 = 0.9998$ ). After several attempts, F1.65 order reaction was determined as the most suitable model. Overall, the activation energy of the three pseudo-components was of the following pattern: lignin + char > cellulose > hemicelluloses (Anca-Couce et al., 2014). This was consistent with the above estimates. The  $R^2$  value of above 0.99 between the estimated and theoretical values at each stage pointed to the accuracy of the combustion mechanism selection (Fig. 9). Since a higher  $E_a$  value means a slower response (Chen et al., 2018), the energy barrier to be overcome was smaller for the PB than PA combustion.

The value of  $A$  can be obtained from the slope of the best-fit linear function of  $\frac{E_a \cdot p(u)}{\beta R}$  versus  $g(\alpha)$  (Table 7). The frequency of the collision between reactants can be represented using  $A$  values.  $A$  values <  $10^9 s^{-1}$  represent a surface reaction but point to a dense complex if the reaction is not dependent on the surface.  $A$  values >  $10^9 s^{-1}$  represent a simpler complex (Yuan et al., 2017).  $A$  values between  $10^{10}$  and  $10^{12} s^{-1}$  show that the rotation of the activated complex may be limited compared to the initial reagent. The mean  $A$  values of the three sub-reactions were  $1 \times 10^{17}$ ,  $8.03 \times 10^{18}$  and  $1.04 \times 10^{20} s^{-1}$  for PA and  $4.04 \times 10^{12}$ ,  $2.33 \times 10^{15}$  and  $4.33 \times 10^{13} s^{-1}$  for PB, respectively. Therefore, both PA and PB had a simpler complex with multiple chemical reactions during the combustion. However, PB broke through the energy barrier more

easily than did PA (Chong et al., 2019).

#### 4. Conclusions

*Pteris vittata* as a rapidly growing, highly productive and widely geo-distributed plant has a relatively higher calorific value and a great potential for a cleaner bioenergy generation. The emissions released were of the following order:  $CO_2 \gg CH_4 > CO \gg NH_3 > H_2 > NO > HCN > NO_2 > SO_2$  from the PA combustion and  $CO_2 > CO > CH_4 \gg NH_3 > H_2 > NO > NO_2 > HCN > SO_2$  from the PB combustion. PA was rich in N and S in the form of reductive intermediates. The PB combustion led to a higher emission level with a more rigid control over its combustion temperature than did the PA combustion. The main combustion stage of devolatilization occurred between 200 and 650 °C for PA and between 200 and 510 °C for PB, with the three major peaks of higher biomass loss for PA than PB. The joint optimization pointed to 999.2 and 514.6 °C, 193.6 and 97.1 min, and 40 °C/min for PB and PA, respectively, as the optimum and cleanest production schemes. The mean  $E_a$  values were 188.60, 214.31, and 272.19 kJ/mol and 135.96, 167.46, and 178.90 kJ/mol for the hemicelluloses, cellulose and lignin + char reactions of PA and PB, respectively. In the future studies, their co-combustion with a range of sludge types and/or alkali metal catalysts remains to be explored for the industrial-scale applications. Reductive intermediates produced by the volatiles combustion of the biomass fuels may be used to reduce  $SO_2$

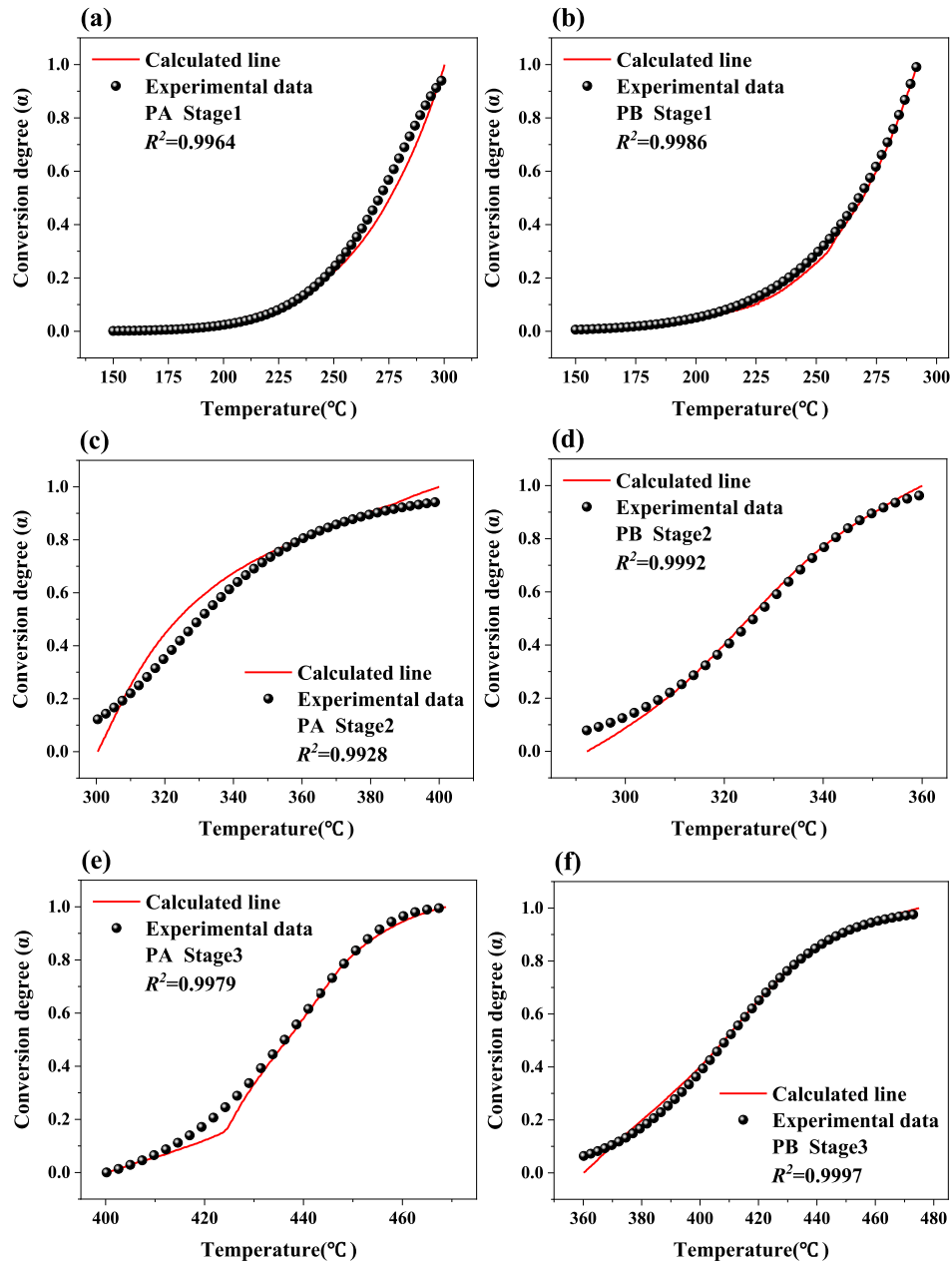


Fig. 9. Comparison of calculated and experimental curves for stages (a–b) 1, (c–d) 2 and (e–f) 3 for PA and PB combustions, respectively.

**Table 7**  
Kinetic triplets of pseudo-components of PA and PB combustions at 20 °C/min.

Reaction stage	$A$ ( $s^{-1}$ )	$E_a$ (kJ/mol)	$f(\alpha)$	$g(\alpha)$	$R^2$	
PA	1	$1.00 \times 10^{17}$	188.60	$[(3/2)(1-\alpha)^{1/3}]/[1-(1-\alpha)^{1/3}]$	$(1-2\alpha/3)-(1-\alpha)^{2/3}$	0.9988
	2	$8.03 \times 10^{18}$	214.31	$(1-\alpha)^3$	$-\ln(1-\alpha)$	0.9960
	3	$1.04 \times 10^{20}$	272.19	$1-\alpha$	$[(1-\alpha)^{-2}-1]/2$	0.9991
PB	1	$4.04 \times 10^{12}$	135.96	$1/2\alpha$	$\alpha^2$	0.9997
	2	$2.33 \times 10^{15}$	167.46	$(1-\alpha)^{13/10}$	$[(1-\alpha)^{-3/10}-1]/(3/10)$	0.9997
	3	$4.33 \times 10^{13}$	178.90	$(1-\alpha)^{33/20}$	$[(1-\alpha)^{-13/20}-1]/(13/20)$	0.9998

emission, and thus, to achieve a cleaner production.

## Acknowledgements

This work was funded by the National Natural Science Foundation of China (no. 51608129), and the Science and Technology Planning Project of Guangdong Province, China (no. 2019CS05307, 2017A050501036, 2018A050506046, and 2019B020208017).

## Appendix A. Supplementary data

Supplementary data to this article can be found online at <https://doi.org/10.1016/j.jclepro.2019.117772>.

## References

- Abid, R., Manzoor, M., De Oliveira, L.M., da Silva, E., Rathinasabapathi, B., Rensing, C., Mahmood, S., Liu, X., Ma, L.Q., 2019. Interactive effects of As, Cd and Zn on their uptake and oxidative stress in As-hyperaccumulator *Pteris vittata*. *Environ. Pollut.* 248, 756–762.
- Anca-Couce, A., Berger, A., Zobel, N., 2014. How to determine consistent biomass pyrolysis kinetics in a parallel reaction scheme. *Fuel* 123, 230–240.
- Bach, Q.V., Tran, K.Q., Skreiberg, O., 2017. Combustion kinetics of wet-torrefied forest residues using the distributed activation energy model (DAEM). *Appl. Energy* 185, 1059–1066.
- Balasundram, V., Ibrahim, N., Kasmani, R.M., Abd Hamid, M.K., Isha, R., Hasbullah, H., Ali, R.R., 2017. Thermogravimetric catalytic pyrolysis and kinetic studies of coconut copra and rice husk for possible maximum production of pyrolysis oil. *J. Clean. Prod.* 167, 218–228.
- Cai, H., Zou, H., Liu, J., Xie, W., Kuo, J., Buyukada, M., Evrendilek, F., 2018. Thermal degradations and processes of waste tea and tea leaves via TG-FTIR: combustion performances, kinetics, thermodynamics, products and optimization. *Bioresour. Technol.* 268, 715–725.
- Cai, H.M., Liu, J.Y., Xie, W.M., Kuo, J.H., Buyukada, M., Evrendilek, F., 2019. Pyrolytic kinetics, reaction mechanisms and products of waste tea via TG-FTIR and Py-GC/MS. *Energy Convers. Manag.* 184, 436–447.
- Chen, J., 2018. Bio-oil production from hydrothermal liquefaction of *Pteris vittata* L.: effects of operating temperatures and energy recovery. *Bioresour. Technol.* 265, 320–327.
- Chen, J., Mu, L., Jiang, B., Yin, H., Song, X., Li, A., 2015. TG/DSC-FTIR and Py-GC investigation on pyrolysis characteristics of petrochemical wastewater sludge. *Bioresour. Technol.* 192, 1–10.
- Chen, J., Wang, Y., Lang, X., Ren, X., Fan, S., 2017a. Comparative evaluation of thermal oxidative decomposition for oil-plant residues via thermogravimetric analysis: thermal conversion characteristics, kinetics, and thermodynamics. *Bioresour. Technol.* 243, 37–46.
- Chen, J., Wang, Y., Lang, X., Ren, X., Fan, S., 2017b. Evaluation of agricultural residues pyrolysis under non-isothermal conditions: thermal behaviors, kinetics, and thermodynamics. *Bioresour. Technol.* 241, 340–348.
- Chen, J., Xie, C., Liu, J., He, Y., Xie, W., Zhang, X., Chang, K., Kuo, J., Sun, J., Zheng, L., Sun, S., Buyukada, M., Evrendilek, F., 2018. Co-combustion of sewage sludge and coffee grounds under increased O<sub>2</sub>/CO<sub>2</sub> atmospheres: thermodynamic characteristics, kinetics and artificial neural network modeling. *Bioresour. Technol.* 250, 230–238.
- Chen, R.Y., Lu, S.X., Zhang, Y., Lo, S.M., 2017c. Pyrolysis study of waste cable hose with thermogravimetry/Fourier transform infrared/mass spectrometry analysis. *Energy Convers. Manag.* 153, 83–92.
- Chong, C.T., Mong, G.R., Ng, J.H., Chong, W.W.F., Ani, F.N., Lam, S.S., Ong, H.C., 2019. Pyrolysis characteristics and kinetic studies of horse manure using thermogravimetric analysis. *Energy Convers. Manag.* 180, 1260–1267.
- Darda, S., Papalas, T., Zabanitouta, A., 2019. Biofuels journey in Europe: currently the way to low carbon economy sustainability is still a challenge. *J. Clean. Prod.* 208, 575–588.
- Dhyani, V., Bhaskar, T., 2018. A comprehensive review on the pyrolysis of ligno-cellulosic biomass. *Renew. Energy* 129, 695–716.
- Duan, L.B., Chen, J., Jiang, Y., Li, X.L., Longhurst, P., Lei, M., 2017. Experimental and kinetic study of thermal decomposition behaviour of phytoremediation derived *Pteris vittata*. *J. Therm. Anal. Calorim.* 128 (2), 1207–1216.
- Fang, S.W., Yu, Z.S., Ma, X.Q., Lin, Y., Lin, Y.S., Chen, L., Fan, Y.L., Liao, Y.F., 2017. Co-pyrolysis characters between combustible solid waste and paper mill sludge by TG-FTIR and Py-GC/MS. *Energy Convers. Manag.* 144, 114–122.
- Guo, F.H., Zhong, Z.P., 2018. Optimization of the co-combustion of coal and composite biomass pellets. *J. Clean. Prod.* 185, 399–407.
- He, F., Yi, W., Bai, X., 2006. Investigation on calorific requirement of biomass pyrolysis using TG-DSC analyzer. *Energy Convers. Manag.* 47 (15–16), 2461–2469.
- Hu, J., Yan, Y., Evrendilek, F., Buyukada, M., Liu, J., 2019. Combustion behaviors of three bamboo residues: gas emission, kinetic, reaction mechanism and optimization patterns. *J. Clean. Prod.* 235, 549–561.
- Hu, M.A., Wang, X., Chen, J., Yang, P., Liu, C.X., Xiao, B., Guo, D.B., 2017. Kinetic study and syngas production from pyrolysis of forestry waste. *Energy Convers. Manag.* 135, 453–462.
- Huang, J., Liu, J., Chen, J., Xie, W., Kuo, J., Lu, X., Chang, K., Wen, S., Sun, G., Cai, H., Buyukada, M., Evrendilek, F., 2018. Combustion behaviors of spent mushroom substrate using TG-MS and TG-FTIR: thermal conversion, kinetic, thermodynamic and emission analyses. *Bioresour. Technol.* 266, 389–397.
- Huang, J., Liu, J., Kuo, J., Xie, W., Zhang, X., Chang, K., Buyukada, M., Evrendilek, F., 2019a. Kinetics, thermodynamics, gas evolution and empirical optimization of (co-)combustion performances of spent mushroom substrate and textile dyeing sludge. *Bioresour. Technol.* 280, 313–324.
- Huang, J., Zhang, J., Liu, J., Xie, W., Kuo, J., Chang, K., Buyukada, M., Evrendilek, F., Sun, S., 2019b. Thermal conversion behaviors and products of spent mushroom substrate in CO<sub>2</sub> and N<sub>2</sub> atmospheres: kinetic, thermodynamic, TG and Py-GC/MS analyses. *J. Anal. Appl. Pyrolysis* 139, 177–186.
- Huang, L., Liu, J., He, Y., Sun, S., Chen, J., Sun, J., Chang, K., Kuo, J., Ning, X., 2016. Thermodynamics and kinetics parameters of co-combustion between sewage sludge and water hyacinth in CO<sub>2</sub>/O<sub>2</sub> atmosphere as biomass to solid biofuel. *Bioresour. Technol.* 218, 631–642.
- Jain, A.A., Mehra, A., Ranade, V.V., 2016. Processing of TGA data: analysis of iso-conversional and model fitting methods. *Fuel* 165, 490–498.
- Lei, M., Dong, Z.P., Jiang, Y., Longhurst, P., Wan, X.M., Zhou, G.D., 2019. Reaction mechanism of arsenic capture by a calcium-based sorbent during the combustion of arsenic-contaminated biomass: a pilot-scale experience. *Front. Environ. Sci. Eng.* 13 (2).
- Liang, F., Wang, R., Hongzhong, X., Yang, X., Zhang, T., Hu, W., Mi, B., Liu, Z., 2018. Investigating pyrolysis characteristics of moso bamboo through TG-FTIR and Py-GC/MS. *Bioresour. Technol.* 256, 53–60.
- Liu, J., Huang, L., Xie, W., Kuo, J., Buyukada, M., Evrendilek, F., 2019. Characterizing and optimizing (co-)pyrolysis as a function of different feedstocks, atmospheres, blend ratios, and heating rates. *Bioresour. Technol.* 277, 104–116.
- Liu, J., Zhuo, Z., Sun, S., Xie, W., Lu, S., Sun, J., Kuo, J., Yujie, W., 2016. Thermal behavior of Cd during sludge incineration: experiments and thermodynamic equilibrium model. *Water Environ. Res.* 88 (12), 2245–2256.
- Magdziarz, A., Gajek, M., Nowak-Woźny, D., Wilk, M., 2018. Mineral phase transformation of biomass ashes – experimental and thermochemical calculations. *Renew. Energy* 128, 446–459.
- Mladenović, M., Paprika, M., Marinković, A., 2018. Denitrification techniques for biomass combustion. *Renew. Sustain. Energy Rev.* 82, 3350–3364.
- Mosevitzky, B., Shter, G.E., Grader, G.S., 2018. Effect of equivalence ratio on the thermal autoignition of aqueous ammonia ammonium nitrate monofuel. *Combust. Flame* 188, 142–149.
- Naqvi, S.R., Jamshaid, S., Naqvi, M., Farooq, W., Niazi, M.B.K., Aman, Z., Zubair, M., Ali, M., Shahbaz, M., Inayat, A., Afzal, W., 2018. Potential of biomass for bioenergy in Pakistan based on present case and future perspectives. *Renew. Sustain. Energy Rev.* 81, 1247–1258.
- Paredes-Sanchez, J.P., Lopez-Ochoa, L.M., Lopez-Gonzalez, L.M., Las-Heras-Casas, J., Xiberta-Bernat, J., 2019. Evolution and perspectives of the bioenergy applications in Spain. *J. Clean. Prod.* 213, 553–568.
- Posom, J., Sirisomboon, P., 2017. Evaluation of lower heating value and elemental composition of bamboo using near infrared spectroscopy. *Energy* 121, 147–158.
- Shah, I.A., Gou, X., Zhang, Q.Y., Wu, J.X., Wang, E.Y., Liu, Y.F., 2018. Experimental study on NO<sub>x</sub> emission characteristics of oxy-biomass combustion. *J. Clean. Prod.* 199, 400–410.
- Shi, Q., Qin, B., Bi, Q., Qu, B., 2018. An experimental study on the effect of igneous intrusions on chemical structure and combustion characteristics of coal in Daxing Mine, China. *Fuel* 226, 307–315.
- Sun, G., Zhang, G., Liu, J., Xie, W., Kuo, J., Lu, X., Buyukada, M., Evrendilek, F., Sun, S., 2019. Thermogravimetric and mass-spectrometric analyses of combustion of spent potlining under N<sub>2</sub>/O<sub>2</sub> and CO<sub>2</sub>/O<sub>2</sub> atmospheres. *Waste Manag.* 87, 237–249.
- Tian, K., Liu, W.J., Qian, T.T., Jiang, H., Yu, H.Q., 2014. Investigation on the evolution of N-containing organic compounds during pyrolysis of sewage sludge. *Environ. Sci. Technol.* 48 (18), 10888–10896.
- Wang, J., Ma, X., Yu, Z., Peng, X., Lin, Y., 2018a. Studies on thermal decomposition behaviors of demineralized low-lipid microalgae by TG-FTIR. *Thermochim. Acta* 660, 101–109.
- Wang, P., Deng, X.Z., Zhang, N., Zhang, X.Y., 2019a. Energy efficiency and technology gap of enterprises in Guangdong province: a meta-frontier directional distance function analysis. *J. Clean. Prod.* 212, 1446–1453.
- Wang, T., Hou, H.B., Ye, Y., Rong, H., Li, J.P., Xue, Y.J., 2019b. Combustion behavior of refuse-derived fuel produced from sewage sludge and rice husk/wood sawdust using thermogravimetric and mass spectrometric analyses. *J. Clean. Prod.* 222, 1–11.
- Wang, Y., Shao, Y.X., Matovic, M.D., Whalen, J.K., 2015. Exploring switchgrass and hardwood combustion on excess air and ash fouling/slugging potential: Laboratory combustion test and thermogravimetric kinetic analysis. *Energy Convers. Manag.* 97, 409–419.
- Wang, Z., Hong, C., Xing, Y., Li, Y., Feng, L., Jia, M., 2018b. Combustion behaviors and kinetics of sewage sludge blended with pulverized coal: with and without catalysts. *Waste Manag.* 74, 288–296.
- Xie, C.D., Liu, J.Y., Xie, W.M., Kuo, J.H., Lu, X.W., Zhang, X.C., He, Y., Sun, J., Chang, K.L., Xie, W.H., Liu, C., Sun, S.Y., Buyukada, M., Evrendilek, F., 2018. Quantifying thermal decomposition regimes of textile dyeing sludge, pomelo peel, and their blends. *Renew. Energy* 122, 55–64.
- Xie, Q.E., Yan, X.L., Liao, X.Y., Li, X., 2009. The arsenic hyperaccumulator fern *Pteris vittata* L. *Environ. Sci. Technol.* 43 (22), 8488–8495.

- Yan, X.-L., Chen, T.-B., Liao, X.-Y., Huang, Z.-C., Pan, J.-R., Hu, T.-D., Nie, C.-J., Xie, H., 2008a. Arsenic transformation and volatilization during incineration of the Hyperaccumulator *Pteris vittata* L. Environ. Sci. Technol. 42 (5), 1479–1484.
- Yan, X.L., Chen, T.B., Liao, X.Y., Huang, Z.C., Pan, J.R., Hu, T.D., Nie, C.J., Xie, H., 2008b. Arsenic transformation and volatilization during incineration of the hyper-accumulator *Pteris vittata* L. Environ. Sci. Technol. 42 (5), 1479–1484.
- Yang, H.P., Yan, R., Chen, H.P., Lee, D.H., Zheng, C.G., 2007. Characteristics of hemi-cellulose, cellulose and lignin pyrolysis. Fuel 86 (12–13), 1781–1788.
- Yuan, X.S., He, T., Cao, H.L., Yuan, Q.X., 2017. Cattle manure pyrolysis process: kinetic and thermodynamic analysis with isoconversional methods. Renew. Energy 107, 489–496.
- Zhang, J., Liu, J., Evrendilek, F., Zhang, X., Buyukada, M., 2019a. TG-FTIR and Py-GC/MS analyses of pyrolysis behaviors and products of cattle manure in CO<sub>2</sub> and N<sub>2</sub> atmospheres: kinetic, thermodynamic, and machine-learning models. Energy Convers. Manag. 195, 346–359.
- Zhang, J.H., Liu, J.Y., Evrendilek, F., Xie, W.M., Kuo, J.H., Zhang, X.C., Buyukada, M., 2019b. Kinetics, thermodynamics, gas evolution and empirical optimization of cattle manure combustion in air and oxy-fuel atmospheres. Appl. Therm. Eng. 149, 119–131.
- Zhang, Y., Liu, Y., Shi, X., Yang, C., Wang, W., Li, Y., 2018. Risk evaluation of coal spontaneous combustion on the basis of auto-ignition temperature. Fuel 233, 68–76.
- Zhang, Y., Wan, X., Lei, M., 2017. Application of arsenic hyperaccumulator *Pteris vittata* L. to contaminated soil in Northern China. J. Geochem. Explor. 182, 132–137.
- Zhuo, Z., Liu, J., Sun, S., Sun, J., Kuo, J., Chang, K., Fu, J., Wang, Y., 2017. Thermogravimetric characteristics of textile dyeing sludge, coal and their blend in N<sub>2</sub>/O<sub>2</sub> and CO<sub>2</sub>/O<sub>2</sub> atmospheres. Appl. Therm. Eng. 111, 87–94.